metals

MDPI

Article

Hydrogen-Assisted Microdamage of Eutectoid Pearlitic Steel in the Presence of Notches: The Tearing Topography Surface

Jesús Toribio

Fracture & Structural Integrity Research Group (FSIRG), University of Salamanca (USAL)
E.P.S., Campus Viriato, Avda. Requejo 33, 49022 Zamora, Spain; toribio@usal.es; Tel.: +34-677566723

Abstract: This paper studies the *hydrogen-assisted microdamage* (HAMD) in fully-pearlitic steel. A detailed analysis is provided of the HAMD region in axisymmetric round-notched samples of high-strength eutectoid pearlitic steel under hydrogen embrittlement environmental conditions. The microscopic appearance and evolution of the hydrogen affected region is analyzed from the initiation (sub-critical) to the fracture (critical) situations. The use of very distinct notched samples and their associated stress distributions in the vicinity of the notch tip allows for a study of the key role of the triaxial stress state on hydrogen diffusion and micro-cracking (or micro-damage). The microscopic appearance of the hydrogen-affected zone (the so-called *tearing topography surface*) resembles *micro-damage*, *micro-cracking* or *micro-tearing* at a *micro*- or *nano*-scale due to hydrogen degradation, thus affecting the notch tensile strength and producing hydrogen embrittlement. A micromechanical model is proposed to explain these hydrogen effects on the material on the basis of the lamellar *micro*- and *nano*-structure of the pearlitic steel.

Keywords: high-strength eutectoid pearlitic steel; stress triaxiality; constraint; multiaxial stress states; hydrogen embrittlement; notch tensile strength; hydrogen-assisted microdamage (HAMD); tearing topography surface (TTS); hydrogen damage topography (HDT)

check for updates

Citation: Toribio, J. Hydrogen-Assisted Microdamage of Eutectoid Pearlitic Steel in the Presence of Notches: The Tearing Topography Surface. *Metals* **2023**, *13*, 1365. https://doi.org/10.3390/met13081365

Academic Editors: Jie Hou, Xiao Zhou and Tomáš Prošek

Received: 20 June 2023
Revised: 17 July 2023
Accepted: 27 July 2023
Published: 29 July 2023

Copyright: © 2023 by the author. Licensee MDPI, Basel, Switzerland. This article is an open access article distributed under the terms and conditions of the Creative Commons Attribution (CC BY) license (https://creativecommons.org/licenses/by/4.0/).

1. Introduction

High-strength eutectoid pearlitic steels are used as (i) constituent materials of rails [1,2] (*pearlitic rail steels*) in mass after hot rolling; (ii) constituent materials of pre-stressed concrete structures, bridge cables and wire ropes in wire form as key elements in civil engineering [3–5] (*cold-drawn pearlitic steel wires*) after hot rolling and cold drawing; and (iii) reinforcement materials in vehicle tires [6,7] in the form of tiny wires after heavy cold drawing (*cold-drawn pearlitic steel wires*).

While pearlitic rail steels do not undergo any mechanical treatment (only heat treatment), in cold-drawn pearlitic steels the cold drawing manufacturing procedure activates a strain hardening mechanism, thereby increasing both the yield strength and the ultimate tensile strength (UTS). The evolution of microstructure in pearlitic steel and its associated changes in strength and ductility during cold drawing were studied in the past by Embury and Fisher [8], Langford [9] and Ridley [10], as well as by Lewandowski and Thompson [11]. These important papers constitute, even nowadays, the key background of micromechanical analyses of pearlitic steels (either cold-drawn or not) and they conform the scientific bases of modern fracture mechanics approaches.

It is also worth mentioning the analyses by Nam and Bae [12], Read et al. [13], Toribio and Ovejero [14–17], Languillaume et al. [18] or Nam et al. [19] on microstructure changes in pearlite after drawing [12–17] or drawing-induced cementite dissolution [18,19]. The utmost importance of cold drawing effects on micromechanical features and fracture behavior is out of doubt.

The summary of such an utmost importance of the effects of cold drawing in pearlite is twofold: on one side, it produces orientation of both microstructural levels (pearlite

colonies and lamellae) in the undoubtedly *hierarchical structure* of pearlitic steels [14–17] and, on the other side, it can trigger local deterioration/degradation phenomena such as drawing-induced cementite dissolution [18,19].

A controversial topic [20–23] is the validity of the Hall-Petch equation to describe the better mechanical performance (increase in yield strength) with the decrease in the size of a characteristic microstructural unit: grain size, particle size, or, in the case of pearlitic steels, colony size or interlamellar spacing, the latter being usually considered as the key microstructural length representing the free distance for a dislocation to move before being blocked by the cementite barrier.

The phenomenon of blocking of free dislocation movement in the ferrite phase by the hardest cementite phase acting as a barrier provokes an increase in material strength. Although in *randomly-oriented pearlite* (e.g., in a rail steel or a hot rolled pearlitic steel bar) the Hall-Petch equation can be valid to fit the strength *versus* material characteristic size, in the case of *oriented pearlite* (e.g., in a heavily cold-drawn steel) the relation between microstructure (represented by a characteristic length such as the pearlite interlamellar spacing) and strength does *not* fit a Hall-Petch equation [22] but an Embury-Fisher law [23] in the case of drawn pearlite, to account for the evident microstructural orientation.

Many papers have dealt with the study of different hardening and strengthening mechanisms after cold-drawing of pearlitic microstructures [24–31]. With regard to fracture (*post-yield*) behavior of pearlitic steels, one can find classical papers by Porter et al. [32], Hyzak and Bernstein [33], Park and Bernstein [34], Alexander and Bernstein [35] and Dollar et al. [36], and more recent works [37–42] dealing with plasticity/yielding behavior, as well as fracture performance.

In the matter of environmentally assisted cracking [43], in addition to pure stress corrosion cracking (SCC) by localized anodic dissolution (LAD), the deleterious phenomenon usually known as hydrogen embrittlement (HE) is harmful in cold-drawn pearlitic steel in the form of prestressing steel wires and cables in service [44–52]. The analyses of such a phenomenon usually were performed in the past from the engineering point of view in the form of fracture mechanics approaches to avoid catastrophic accidents (an important practical aspect of HE and HAMD in high-strength pearlitic steel), so that there is a lack of purely-scientific material science approaches.

Such a phenomenon has received many names in the scientific literature such as hydrogen degradation (HD), hydrogen-assisted fracture (HAF) or hydrogen-assisted cracking (HAC) when a crack is present in the material. The first term (HD) is especially important because it includes any deleterious effect caused by hydrogen on a specific material, either typical (pure) embrittlement in the form of lack of ductility or decrease in fracture toughness, or more complicated phenomena involving a sort of interplay between locally ductile processes (localized plasticity or hydrogen-dislocation interactions) and global material degradation.

In this paper, the *hydrogen-assisted microdamage* (HAMD) in the form of the so-called *tearing topography surface* (TTS), a term coined by Thompson and Chesnutt [53] and Costa and Thompson [54] but just described as a new, non-conventional, fractographic mode but, in principle, not associated with a fracture phenomenon of specific nature (either brittle or ductile) or linked to a particular material (although all provided examples deal with metals and alloys).

At the *macro*-, *micro*- and *nano*-levels, the TTS fractographic mode has been associated [55–59] with HE/HD processes and HAMD in pearlitic steel, such a relationship thoroughly analyzed by Toribio (the author of the present paper) and co-workers. The present work goes further in the brief analysis on HE and HAMD in the presence of notches (*hydrogen-assisted notch-induced fracture* and *notch tensile strength*) published in a short paper included in conference proceedings [60].

2. Phenomenological Evidence of HE/HD of Eutectoid Pearlitic Steels at the *Macro*-, *Micro*- and *Nano*-Scales

This section of the paper presents a compendium of evidence of many phenomena of hydrogen embrittlement (HE) or hydrogen degradation (HD) of fully-pearlitic steel in the presence of geometrical defects (or stress concentrators) such as cracks or notches, in the form of a small review (collection) of phenomenological facts providing experimental evidence [55–59] of the association between the non-conventional fractographic mode that has received the name *tearing topography surface* (TTS), cf. [53,54] and the HE/HD of fully-pearlitic steels at the *macro*-, *micro*- and *nano*-scales.

The TTS is a new fracture topography undoubtedly associated with (or linked to) HE/HD (at the macro-scale) and HAMD (at the micro-scale) in pearlitic steel produced by the combined action of mechanical stress-strain fields and chemical/environmental effects (in particular, hydrogen effects in pearlite). There is clear experimental evidence of the association between the TTS region and the hydrogen damage in pearlite, at the macro-, micro- and nano scales, i.e., considering the three levels of hydrogen-assisted damage in the pearlitic material: *macro-damage*, *micro-damage* and *nano-damage*.

The experimental evidence of such an association is as follows [55–59]:

- The microscopic appearance of the TTS region (fractography) clearly resembles *micro-damage* (at the micro-scale) or *nano-damage* (at the nano-scale) consisting of a sort of micro-cracking or micro-tearing due to hydrogen micro- or nano-degradation in pearlite at the finest level of analysis by scanning electron microscopy (SEM).
- The micromechanical behavior of the TTS region (microfracture mode) is manifested by a low crack growth rate (CGR), i.e., it is a slow (or subcritical) crack growth fractography linked to the stage II (*plateau*) in the crack growth kinetics (CGK) curve da/dt-K in which the CGR is independent of the stress intensity factor (SIF K).
- The appearance of the TTS mode/fractography takes place *only* when the electrochemical environment surrounding the pearlitic steel is *cathodic*. In this case of cathodic potential, the predominant phenomenon in the steel is HE/HD in the presence of notches, or hydrogen-assisted cracking (HAC) in the presence of cracks.
- The size of the TTS zone (region/domain), or the depth of such a zone considered as a cracked area, increases as the electro-chemical potential becomes more cathodic, a consequence of the higher amount of hydrogen at the specimen surface available for hydrogen diffusion toward the inner points.
- The size of the TTS zone (region/domain), or the depth of such a zone considered as a cracked area, slightly increases as the acidity of the solution rises, i.e., as the pH lowers because the hydrogen concentration at the sample boundary (crack or notch tip) increases in the cases of smaller (more acid) pH values.
- The size of the TTS zone (region/domain), or the depth of such a zone considered as a cracked area, clearly decreases as the fatigue pre-cracking level (intensity) increases in a pre-cracked sample, as a consequence of the presence of compressive residual stresses near the crack tip induced during fatigue pre-loading.
- The size of the TTS zone (region/domain), or the depth of such a zone considered as a cracked area, significantly increases with the HE test duration (time to failure), i.e., it clearly decreases as the applied strain rate increases, on the basis of a mechanism of transport by stress-assisted hydrogen diffusion with time derivatives.
- The size of the TTS zone (region/domain), or the depth of such a zone considered as a cracked area, depends on the sample geometry through the hydrostatic stress distribution in the specimen. It is consistent with an association between the TTS mode and the HE/HD process on the basis of stress-assisted hydrogen diffusion.
- The asymptotic depth of the TTS region for quasi-static tests (slow enough to allow the stationary condition for the hydrogen diffusion problem to be achieved) reaches the point of maximum hydrostatic stress in the sample, which confirms that hydrogen diffuses towards the points of maximum hydrostatic stress.

3. Experimental Program

A high-strength eutectoid pearlitic steel was used, whose chemical composition is given in Table 1 and whose mechanical properties are as follows: elastic modulus E = 199 GPa, yield strength σ_Y = 600 MPa, ultimate tensile strength (UTS) σ_Y = 1151 MPa. It is a *fully-pearlitic steel* (100% pearlite) exhibiting a coarse pearlitic microstructure, with a pearlite interlamellar spacing of 0.3 μm, an average size of the cleavage facet of 75 μm, and an average pearlite colony size of about 15 μm.

Table 1. Chemical composition (wt %) of the steel.

C	Mn	Si	P	S	Cr	Ni	Mo
0.85	0.60	0.26	0.010	0.030	0.02	0.02	0.001

In this paper, four axisymmetric round-notched geometries were used with a circular notch shape and varying depths and radii, as sketched in Table 2 and Figure 1 so as to achieve very distinct stress triaxiality (constraint) levels in the close vicinity of the notch tip. The external diameter was *D* = 11.25 mm in all specimens after preparation by careful machining to avoid axial curvature and facilitate the alignment of the specimens. Testing under axial displacement was performed using a universal testing machine with fixed grips to guarantee sample alignment and to avoid undesired rotation (i.e., boundary conditions corresponding to imposed axial displacement at the sample ends).

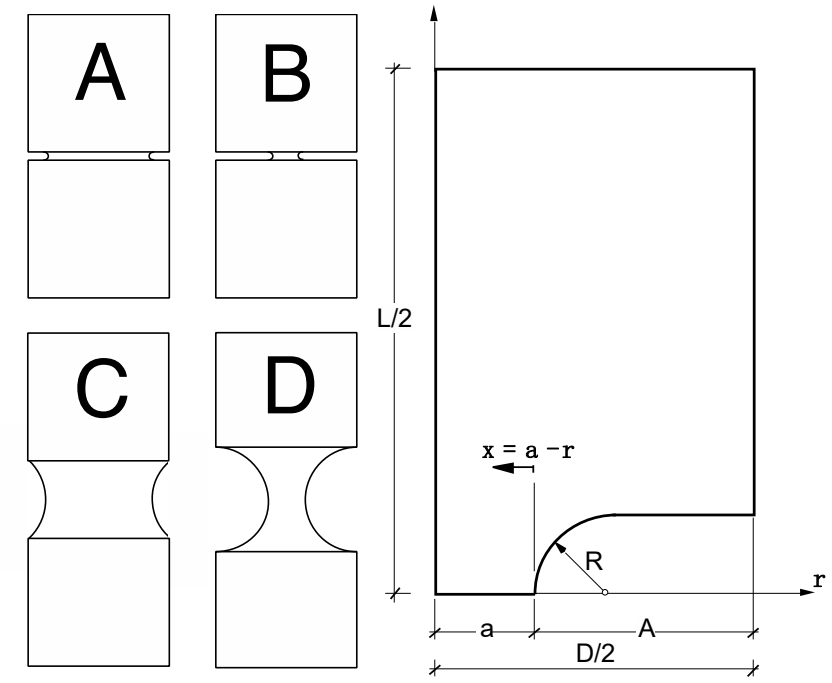


Figure 1. Drawing of axisymmetric notched geometries used in the experiments.

Table 2. Dimensions of the samples and triaxiality levels in all of them.

Sample	R/D	A/D	T
A	0.03	0.10	0.9
B	0.05	0.39	1.4
C	0.36	0.10	0.5
D	0.40	0.39	0.4

R: notch radius, A: notch depth; D sample diameter. (D = 11.25 mm for all specimens, after machining).

To have a reference for comparison, a first set of fracture tests in air was performed on the four notched geometries described above. In addition, HE tests were carried out at room temperature using the same specimens. The samples were subjected to slow strain rate testing (SSRT) with externally-applied displacement rates ranging between 10^{-10} and 2.10^{-6} m/s. The test environment was an aqueous solution of 1 g/L $Ca(OH)_2$ plus 0.1 g/L NaCl. The pH value was 12.5 and tests were performed at a constant electro-chemical potential of −1200 mV SCE (*saturated calomel electrode*) to achieve HE environmental conditions. The advantages of notched geometries in fracture tests in air and in hydrogen environments have been emphasized in the past [60–62] to analyze HE processes and notch tensile strength. The results of the HE tests are given in Table 3.

Table 3. Results of the HE tests.

Sample	u_R (m/s)	t_C (s)	F_H/F_0	x_{HAMD} (mm)
A10	4.79×10^{-7}	555	0.79	0.10
A3	4.81×10^{-7}	570	0.80	0.10
A9	1.82×10^{-7}	1365	0.77	0.15
A4	3.68×10^{-8}	5370	0.70	0.30
A7	3.96×10^{-9}	39,960	0.63	0.34
A1	3.26×10^{-9}	48,600	0.63	0.34
B6	1.00×10^{-7}	720	0.86	0.20
B10	1.03×10^{-7}	780	0.90	0.20
B1	1.02×10^{-8}	5760	0.79	0.25
B9	8.70×10^{-9}	7380	0.82	0.21
B7	6.90×10^{-9}	8520	0.79	0.27
B3	6.23×10^{-9}	11,160	0.85	0.30
B23	6.02×10^{-10}	75,600	0.69	0.60
B22	1.87×10^{-10}	143,040	0.48	0.93
B21	1.12×10^{-10}	262,800	0.52	1.00
C6	1.83×10^{-6}	516	0.91	0.40
C8	9.71×10^{-7}	972	0.91	0.45
C12	3.45×10^{-7}	2295	0.87	0.40
C2	1.54×10^{-7}	4500	0.84	0.55
C11	6.67×10^{-8}	7560	0.77	0.55
C4	5.47×10^{-8}	8340	0.75	0.50
C1	5.85×10^{-9}	68,400	0.72	0.85
C7	5.33×10^{-9}	75,000	0.72	0.75
D10	2.13×10^{-7}	660	0.91	0.10
D3	2.06×10^{-7}	780	0.95	0.21
D7	4.55×10^{-8}	3240	0.92	0.33
D11	2.45×10^{-8}	6300	0.93	0.41
D5	1.49×10^{-8}	9000	0.90	0.60
D2	1.35×10^{-8}	9420	0.88	0.50
D21	6.98×10^{-10}	182,400	0.88	1.15
D24	3.93×10^{-10}	324,000	0.88	1.20

u_R: remote displacement rate. t_C: time to failure or critical time. F_H/F_0: failure load in hydrogen/failure load in air. x_{HAMD}: depth of the hydrogen-assisted micro-damage zone.

4. Fractographic Analysis at the *Macro-*, *Micro-* and *Nano*-Scales

In the tests performed *in air* [63], scanning electron microscope (SEM) fractographic analysis showed that the fracture process always initiates in a *fibrous* or *dimpled* region by a mechanism of *micro-void coalescence* (MVC) and later propagates in an unstable manner by a *cleavage-like* (C) micro-mechanism in geometries A, B and C, or in stable manner by MVC followed by shear lip (L) in the case of geometry D.

To have a complete picture of the fracture process at the micro-mechanical level of pearlitic steel in the presence of notches of very different geometries (with very distinct constraint/triaxiality levels), *micro-fracture maps* (MFMs) were assembled covering the whole fracture surface of all geometries and containing information on the micromechanisms of fracture at each portion of the cross-sectional area (Figure 2).

The macroscopic fracture mode is peripheral and plane in the first case (geometries A, B and C) and central with *cup and cone* shape in the second case (geometry D). The cleavage-like topography associated with unstable final fracture exhibits the typical river patterns indicating the direction and sense of fracture propagation and therefore can explain the different stages of fracture (see Figure 2).

In the case of the first set of geometries exhibiting the most brittle fracture mode (geometries A, B, and C containing the main area of cleavage/brittle fracture in the cross-sectional area, cf. Figure 2), the cleavage micro-fracture mode is *oriented cleavage* in the case of samples A and C (*single fracture initiation point*) and *randomly-oriented cleavage* sample B (*multiple or extended fracture initiation locations*).

A characteristic value of triaxiality seems to exist below which fracture is by MVC and above which it is cleavage-like. This is consistent with the existence of a critical size of micro-void that is a decreasing function of the triaxiality.

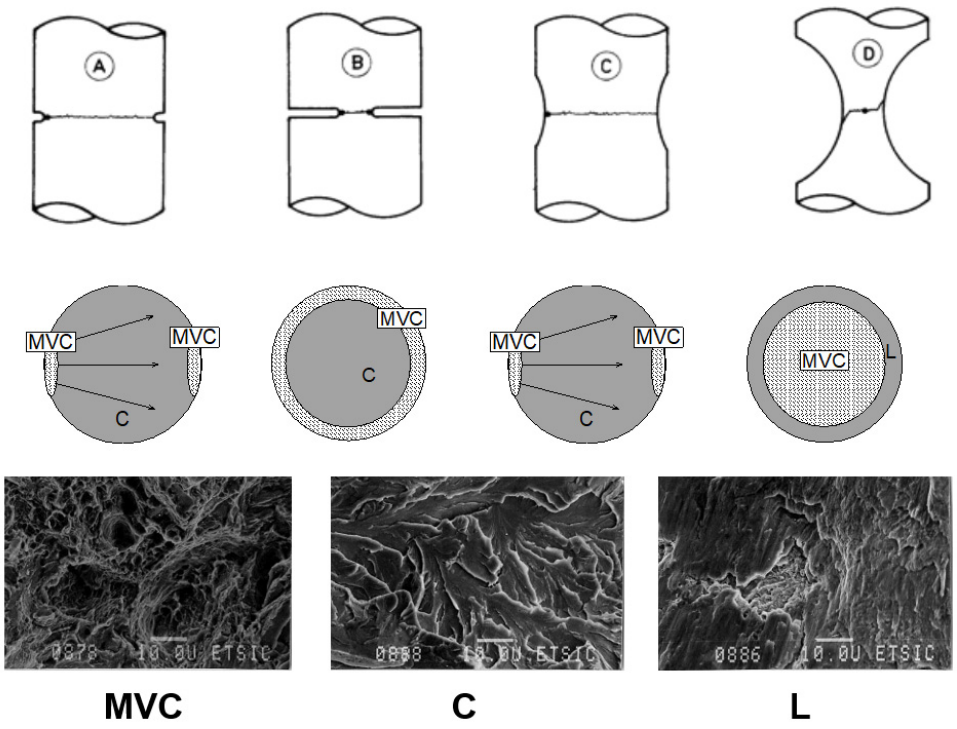


Figure 2. Micro-fracture maps (MFMs) at the fracture in air for the different notched specimens A, B, C and D with very distinct triaxiality levels; MVC: *micro-void coalescence*; C: cleavage-like topography; L: *shear-lip*.

In the HE tests, HAMD started at the notch tip, and fractographic analysis by SEM showed a characteristic microscopic fracture mode (non-conventional) with a kind of ductile tearing appearance: the so-called *tearing topography surface* or TTS (Figure 3), cf. [53–59]. Such a TTS region may be analyzed at the *macro*-, *micro*- and *nano*-levels. To this end, Figure 3 also includes the fully-pearlitic microstructure of the steel, showing the importance of the *nano*-scale, considering the level of the pearlite interlamellar spacing (0.3 μm), i.e., a *sub-micron* scale for the softer (and more ductile) ferrite constrained between harder (and more brittle) cementite, thus allowing a consideration of the fully-pearlitic steel under study as a real *nano*-composite material.

At the *macro-scale*, the TTS zone or domain is a portion of area (region) in the MFM including all fractographic modes in the fracture surface. The MFMs corresponding to the HE tests are given in Figure 4, showing that the TTS region is always peripherical, but in some cases it has thumbnail shape (shallow geometries A and C, either shallow sharp A or shallow blunt C) and in other cases it has a ring shape (deep geometries B and D, either deep sharp B or deep blunt D).

A question should be raised here regarding the macro- and micro-levels of analysis. The concept of MFM corresponds to the macro-scale, since such a map covers the whole macro-fracture surface (circular cross-sectional area of the notched sample in this case). Therefore, it is a macroscopic map containing microscopic modes of fracture, i.e., a map of micro-fracture or *micro-fracture map* (MFM).

After this origin by TTS (environmentally-assisted sub-critical cracking), a fracture progresses in an unstable manner by a cleavage-like (C) topography. In shallow geometries A and C with local thumbnail TTS shape, cleavage develops in a divergent progression and lines form the initiation by TTS, whereas in deep geometries B and D with external circumferential shape by TTS, cleavage progresses towards the inner point of the sample in a random manner (following diverse directions).

A plausible explanation of the type of MFM in each case of Figure 4 would be the following: in sharply-notched geometries A and B, the intense stress concentration produced by the sharp notch creates a maximum of hydrostatic stress near the notch tip, thereby "pumping" hydrogen to locations in the near-tip zone and thus creating the *worst area* (the *most damaged region)* as a local TTS zone placed just at the specimen surface in the form of either a surface crack (sample A) or a surface external ring (sample B).

The same happens in shallow blunt notch C in which the maximum hydrostatic stress is also near the notch tip and thus a thumbnail TTS sub-critical crack is created at the notch tip. With regard to the deep blunt notch D, it exhibits a surface external ring by TTS. In this case, the maximum hydrostatic stress is achieved at the sample axis (place towards which hydrogen diffuses along radial directions), in such a manner that the axial (radial) symmetry is preserved in this case.

Thus, the two shallow geometries (A and C) promote a loss of axial symmetry in the HAMD area with external (surface) thumbnail TTS region whereas the two deep geometries (B and D) preserve the axial symmetry in the HAMD area with external (surface) ring-shaped TTS region.

At the *micro-scale*, the TTS zone contains features resembling micro-damage, micro-cracking or micro-tearing (Figure 3), since it does not have a purely brittle appearance (at the micro-level), in spite of the fact that it is associated with embrittlement by hydrogen (hydrogen embrittlement/HE) in pearlitic steels at the macro-level, so that it is more adequate to speak about hydrogen degradation (HD) in pearlitic steels. At the micro-scale, the TTS zone can be qualified as hydrogen-assisted microdamage (HAMD). The TTS fractography appearing in Figure 3 does not show any evidence of orientation or alignment in privileged direction, i.e., it is randomly oriented. This is the most frequent situation regarding the TTS area (*non-oriented* or *randomly oriented* TTS).

At the *nano-scale*, the TTS region also contains some evidence of tear ridges at the sub-micron level, i.e., at the *nano*-level; it is the level of the pearlite interlamellar spacing of the considered pearlitic steel (about 0.3 μm, i.e., 300 nm). A plausible explanation of this sort of *hydrogen-assisted sub-micron nano-damage* inside the pearlitic microstructure could be any local plasticity/yielding phenomenon related to movement of dislocations along a glide plane in the ferrite phase, with possible breaking of the cementite lamellae by a *nano*-shear mode or by *nano*-tearing mode.

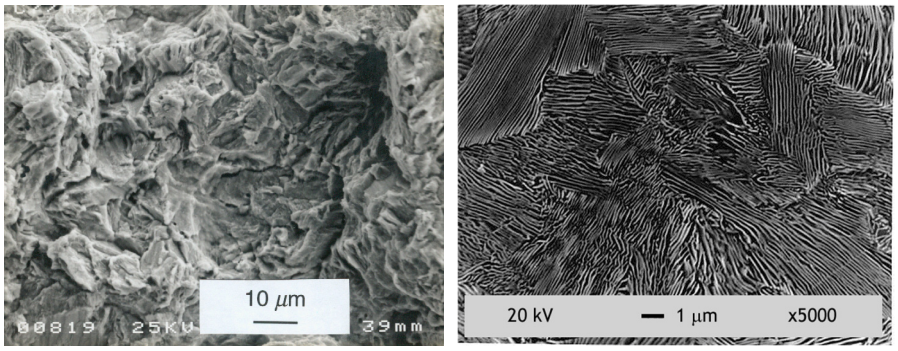


Figure 3. *Tearing topography surface* (TTS) and fully-pearlitic microstructure of the steel.

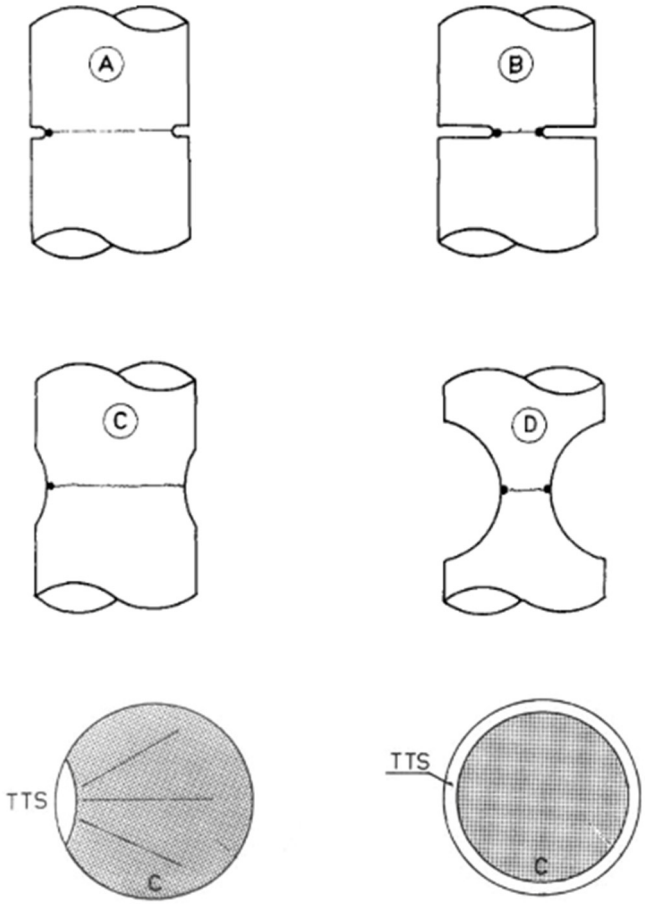


Figure 4. Micro-fracture maps (MFMs) at the fracture in the HE tests for the different notched specimens A, B, C and D with very distinct triaxiality levels; TTS: *tearing topography surface*; C: *cleavage-like topography*.

5. Evolution of Hydrogen-Assisted Microdamage (HAMD)

This section of the paper includes a thorough study on the microscopic features of the HAMD area in the different notched specimens (with distinct triaxiality/constraint level) and its time evolution. Figure 5 shows the microscopic fracture mode in specimen A10, i.e., that of minimum notch depth and minimum notch radius that has undergone the fastest HE experiment (HE test of about 10 min up to final fracture under a hydrogen environment). The fractograph in Figure 5 shows subcritical fracture initiation and slow initial cracking/damage/fracture propagation produced by unconventional TTS (assisted by hydrogen) and critical (unstable) cracking/fracture quick propagation taking place in

the form of a typical cleavage-like micro-fracture mode that is purely mechanical and not assisted by hydrogen. In the slowest test A1 (test duration of about 13.5 h up to final fracture), the micro-fracture map is similar (TTS plus cleavage), but the depth of the HAMD area is higher.

The cleavage-like (C) fractographic mode exhibits the *typical river* patterns signaling the direction of fracture propagation. Such river patterns are *globally divergent* from the area associated with fracture sub-critical initiation by TTS (from bottom to top) and at the same time they are *locally convergent* (in the same way as tributaries approaching the main river flow) in specific areas of the fracture topography (following the sense of fracture propagation direction from the bottom of the fractograph to the top of it). While the TTS fractographic mode represents a sub-critical (hydrogen-assisted) fracture mode associated with slow crack growth, the cleavage-like propagation is quick and unstable while approaching final catastrophic fracture.



Figure 5. Evolution of HAMD in sample A10 (from bottom to top): TTS + cleavage.

Figure 6 presents three fracture areas inside the sample B6, i.e., that of maximum notch depth and minimum notch radius and the fastest HE experiment with a relatively short test duration (time to final fracture of 12 min). At the notch tip (initiation of HAMD) a sort of *orientation* of the TTS topography (*oriented* TTS) may be observed, with an orientation along a radial axis representing the micro-damage (or nano-damage) propagation direction. Such an orientation inside the TTS zone is less defined in areas placed far from the notch tip where the fractographic mode becomes *randomly-oriented* TTS (*non-oriented* TTS in Figure 6c).

After the two TTS regions (*oriented* and *randomly oriented*) that are clearly assisted by hydrogen, the microscopic fracture mode evolves in such a manner that it becomes more similar to the *micro-void coalescence* (MVC) topography (probably also produced with hydrogen assistance) and thus it will be denoted as *quasi-MVC* (QMVC) micro-fracture mode throughout this article, cf. Figure 6a,c, and finally catastrophic fast failure takes place by cleavage (C) with no need of hydrogen assistance (it is quick/brittle mechanical final fracture), as shown at the top of Figure 6a. Figure 6b offers an enlarged and detailed view of the TTS fractographic mode. In the slowest test B21 (with 73 h of test duration up to final fracture), the micro-fracture map (MFM) is similar (TTS plus QMVC plus cleavage), but the depth of the HAMD area is higher in this case.

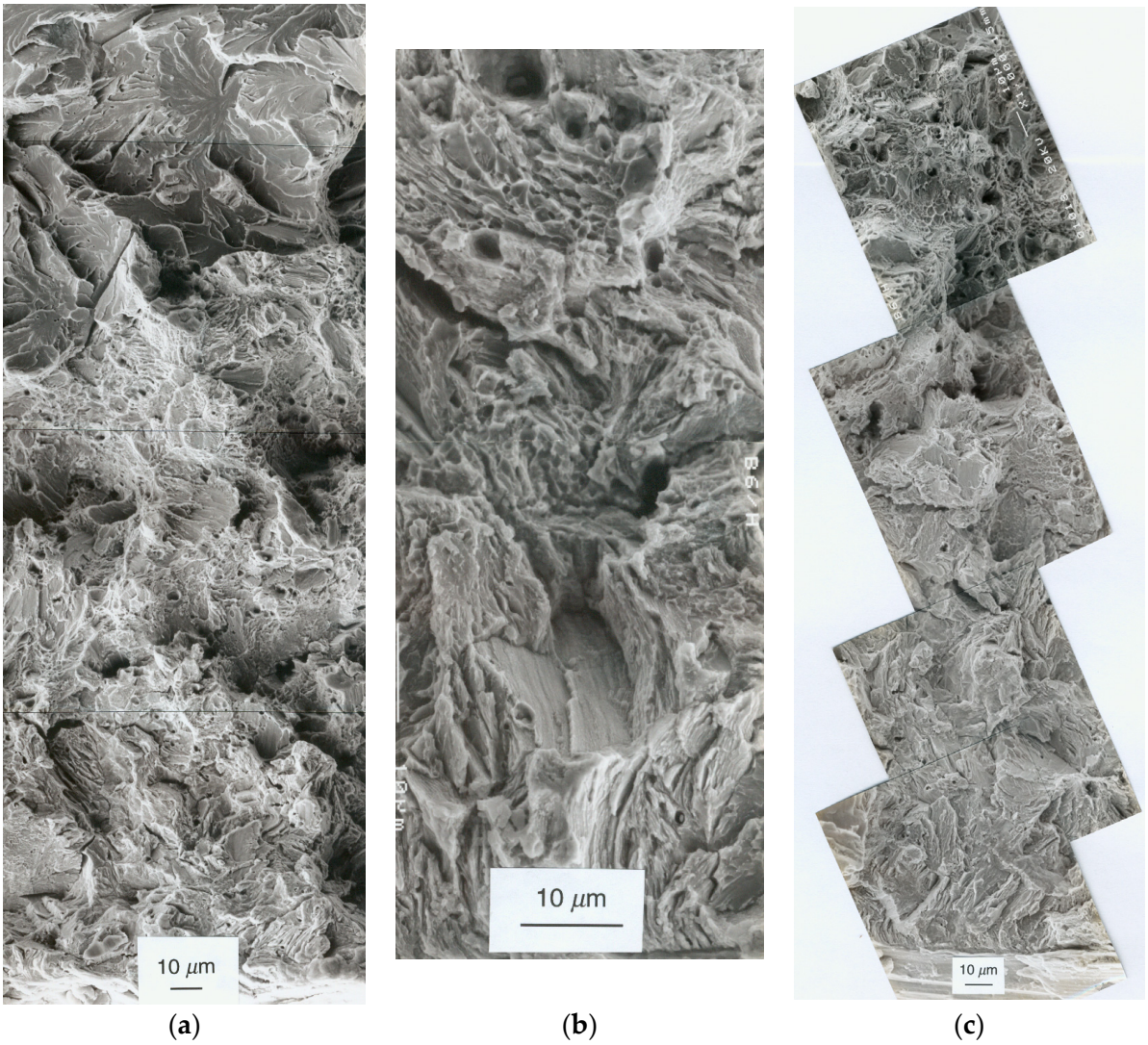
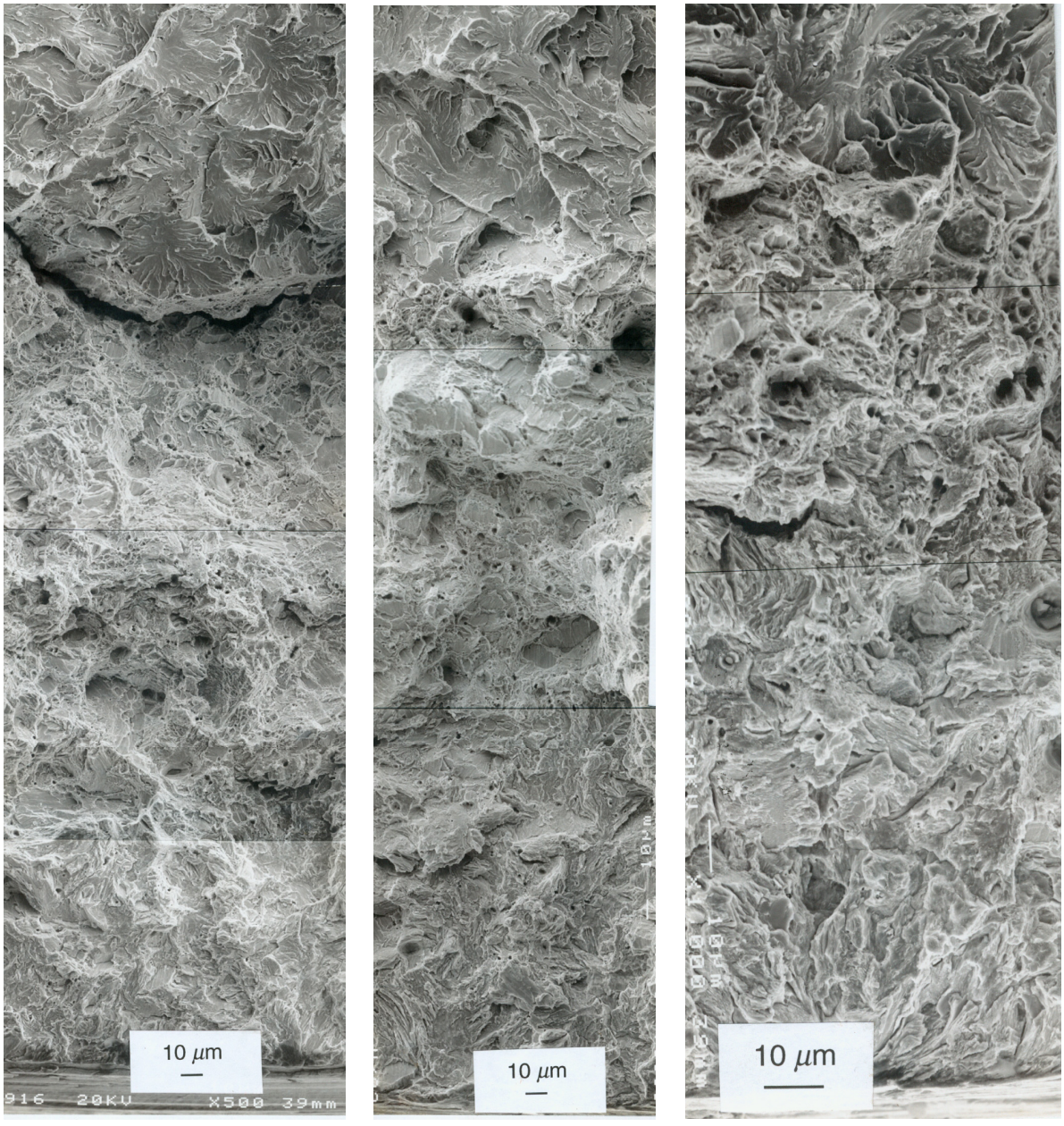


Figure 6. Evolution of HAMD in different locations of specimen B6: (**a**) initiation of HAMD by TTS followed by quasi-MVC and C; (**b**) enlarged view of the TTS microscopic topography in the close vicinity of the notch tip (at the bottom of the fractograph itself); (**c**) different HAMD sub-modes, namely, initiation of HAMD by *oriented* TTS which turns to *non-oriented* TTS and to quasi-MVC. *Fracture propagation from bottom to top in all fractographs.*

Figure 7 describes the evolution of HAMD in specimen C6, i.e., that of minimum notch depth and maximum notch radius (with a duration of 9 min in the HE test; i.e., the fastest experiment for this geometry). The sequence of fracture events is as follows: (i) slow (sub-critical) initiation of hydrogen-assisted fracture/cracking by *oriented* TTS;

(ii) further slow progress by *randomly oriented* TTS (*non-oriented* TTS) that is also assisted by the hydrogen environment and sub-critical; (iii) final slow fracture development by a *poorly-defined* quasi-MVC (probably with certain hydrogen assistance); (iv) final quick fracture (catastrophic/unstable) by cleavage (C) with no need of environmental (hydrogen) assistance. In this geometry C, it is important to emphasize that, in the slowest HE test C7 (21 h of test duration up to final fracture), the micro-fracture map (MFM) is different (TTS plus cleavage), i.e., the QMVC area *disappears* in this case, apart from the fact that the depth of the HAMD area is higher.



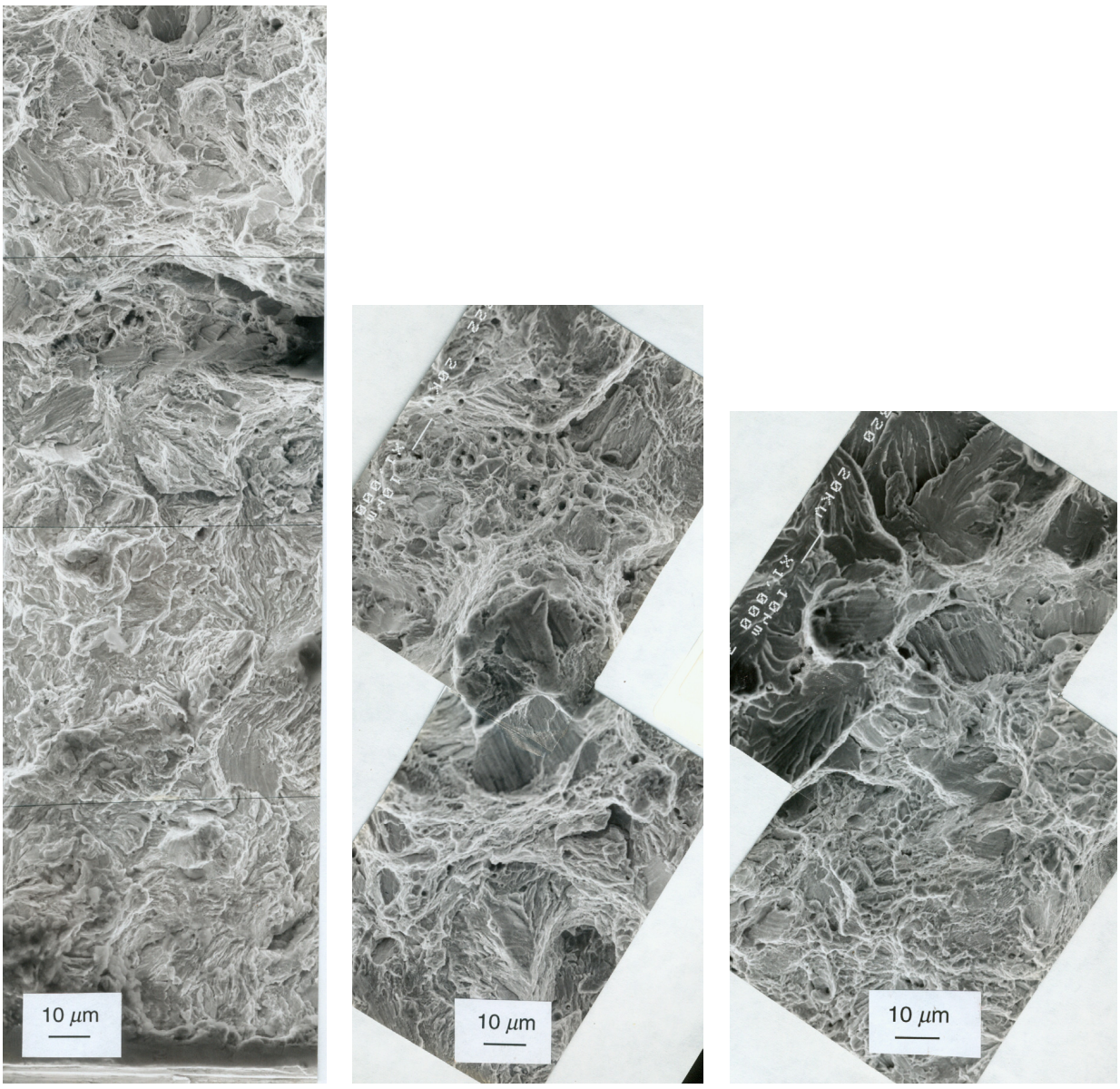
(**a**) (**b**) (**c**)

Figure 7. Evolution of HAMD in different locations of specimen C6: (**a**) initiation of HAMD by TTS followed by quasi-MVC and C; (**b**) initiation of HAMD by TTS followed by quasi-MVC and C (the initiation by TTS is well defined in this specific fracture zone); (**c**) initiation of HAMD by *oriented* TTS which turns to *non-oriented* TTS and to *poorly-defined* quasi-MVC, before final fracture by C. *Fracture propagation from bottom to top in all fractographs*.

Figure 8 corresponds to specimen D5, i.e., that of maximum notch depth and maximum notch radius with an intermediate HE test duration of 2.5 h up to final fracture. The same trends of evolution of HAMD are observed, i.e., the following sequence (Figure 8a):

oriented TTS → *randomly oriented* TTS → quasi-MVC

The transition from TTS to quasi-MVC (specimen D5) is given in Figure 8b and the transition from quasi-MVC to cleavage (also in specimen D5) is shown in Figure 8c. With the same bluntly-notched geometry D and the slowest test D24 (with a long test duration of 90 h up to final fracture) the micro-fracture map (MFM) is similar (TTS plus QMVC plus cleavage) but the depth of the HAMD area is higher in this case.



(**a**) (**b**) (**c**)

Figure 8. Evolution of HAMD in different locations of specimen D5: (**a**) *oriented* TTS → *randomly-oriented* TTS → quasi-MVC; (**b**) transition from TTS to quasi-MVC; (**c**) transition from quasi-MVC to cleavage. *Fracture propagation from bottom to top in all fractographs*.

To complete the information about the TTS features, Figure 9 shows the initiation of HAMD by TTS in the annular external ring of sample D10, i.e., that of maximum notch depth and maximum notch radius with the minimum test duration of 11 min. Hydrogen damage at the micro-level can be observed in the external circumferential ring, in spite of the short duration of the test.



Figure 9. Initiation of HAMD by TTS in the annular external ring of sample D10 (*fracture propagates from left to right*).

In the matter of the triaxiality effects on HAMD of the pearlitic steel considered in the present paper and its dependence and evolution with the embrittlement time, the fractographic features at the *macro*-, *micro*- and *nano*-scales in all notched geometries should be analyzed considering two limit experiments: (i) *quasi-instantaneous tests* (short enough to avoid deep hydrogen penetration distances from the notch tip) and, on the other hand, (ii) *quasi-static tests* (long enough to allow the stationary condition for the hydrogen diffusion problem to be reached, thus permitting deep hydrogen penetration distances from the notch tip). The embrittlement time for the quasi-instantaneous tests was about 10 min, whereas for quasi-static experiments, such a time (test duration) ranged from 10 to 100 h (see Table 3).

Table 4 shows the progression of HAMD in the considered pearlitic steel for distinct triaxiality levels in the specimen geometry. The transition region between the TTS and the cleavage areas in the form of quasi-MVC fracture zone appears *only* in certain cases: firstly, in geometries containing deep notches, either a sharp deep notch (geometry B) or a blunt deep notch (geometry D), in both cases of short and long HE tests; secondly, the

quasi-MVC topography also appears in geometry C containing a blunt shallow notch (but the quasi-MVC are appears *only* in the case of short HE tests).

In other words, the quasi-MVC zone disappears (and all the HAMD region is pure TTS) for the geometry A (with a sharp shallow notch) and for long tests on geometry C (blunt shallow notch), and it becomes less defined for long tests of geometry B (sharp deep notch) and for short tests of geometry C (blunt shallow notch). In the next section, this effect is analyzed on the basis of the hydrostatic stress distribution in the different notched specimens used in the experiments.

Table 4. Triaxiality and time evolution of hydrogen-assisted micro-damage (HAMD).

Geometry	Duration	Fractography
A	short	TTS + C
A	long	TTS + C
B	short	TTS + QMVC + C
B	long	TTS + (QMVC) + C
C	short	TTS + (QMVC) + C
C	long	TTS + C
D	short	TTS + QMVC + C
D	long	TTS + QMVC + C

TTS: tearing topography surface. QMVC: quasi-micro-void coalescence. (QMVC): Idem, when it is short or ill-defined. C: cleavage-like.

6. Continuum Mechanics Approach

6.1. Hydrogen Diffusion Assisted by Stress and Strain

Hydrogen embrittlement (HE) or, using a more general term, hydrogen degradation (HD) is a process of material deterioration by the harmful effect of hydrogen, and it requires hydrogen transport by diffusion from the external surface (notch tip) towards the prospective fracture sites, and such a diffusion is assisted by both the stress and the strain fields in the material (*stress-and-strain-assisted diffusion of hydrogen*). The hydrogen flux depends of several terms, namely: the gradient of hydrogen concentration, the gradient of hydrostatic stress (σ) and the gradient of hydrogen solubility ($K_{s\varepsilon}$) that is itself a function of the equivalent plastic strain ε_p [64]:

$$\mathbf{J} = -D(\bar{\varepsilon}_p)\left\{\nabla C - C\left[\frac{V_H}{RT}\nabla\sigma + \frac{\nabla K_{S\varepsilon}(\bar{\varepsilon}_p)}{K_{S\varepsilon}(\bar{\varepsilon}_P)}\right]\right\}, \quad (1)$$

J being the hydrogen flux, D the diffusion constant, C the hydrogen concentration, R the molar gas constant, V_H the partial volume of hydrogen, T the absolute temperature and $K_{s\varepsilon}$ the hydrogen solubility.

The hydrogen diffusion equation is as a second-order partial differential equation obtained by applying the matter conservation law and the Gauss-Ostrogradsky theorem, resulting in:

$$\frac{\partial C}{\partial t} = \nabla\cdot\left[D\nabla C - DC\left(\frac{V_H}{RT}\nabla\sigma + \frac{\nabla K_{S\varepsilon}(\bar{\varepsilon}_P)}{K_{S\varepsilon}(\bar{\varepsilon}_P)}\right)\right]. \quad (2)$$

Thus, from Equation (2), the effect on hydrogen diffusion of the three driving forces is easily understandable. Hydrogen diffuses towards the inner points due to: (i) the negative gradient of hydrogen concentration (similar to Fick's law); (ii) the positive gradient of hydrostatic stress; (iii) the positive gradient of hydrogen solubility, which is a function of the gradient of equivalent plastic strain.

The concentration of hydrogen for long times of exposure, C_{eq} (equilibrium state reached for infinite time) can be obtained by the following steady-state solution of differential Equation (2) in a well-known Maxwell-Boltzman type:

$$C_{eq} = C_0 K_{S\varepsilon}(\bar{\varepsilon}_P) \exp\left[\frac{V_H}{RT}\nabla\sigma\right], \quad (3)$$

where C_0 is the equilibrium hydrogen concentration for the material free of stress and strain.

Figure 10 shows a scheme of the influence on hydrogen diffusion of the driving forces according to the aforementioned model of diffusion assisted by stress and strain fields [64].

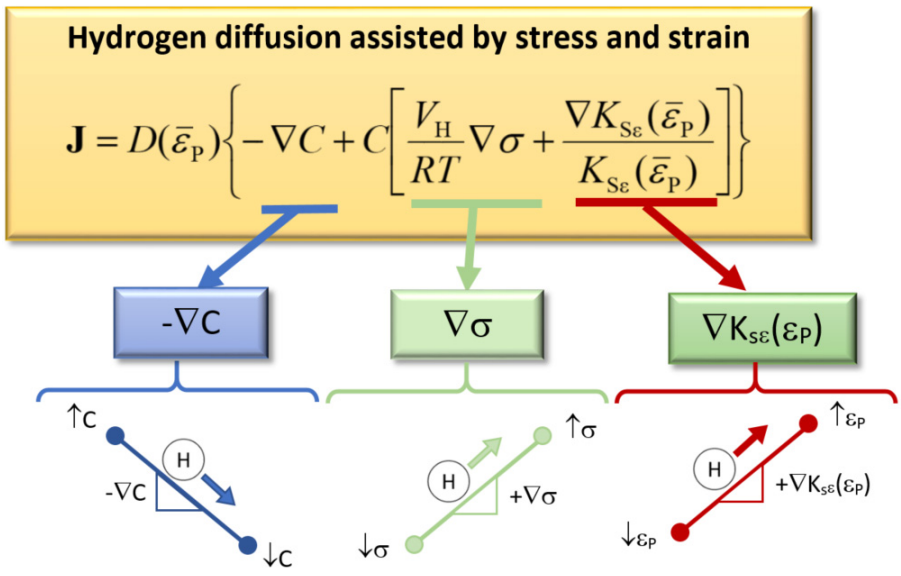


Figure 10. Scheme of the influence on hydrogen diffusion of the driving forces according to the model of diffusion assisted by stress and strain. It is the keystone in the continuum mechanics approach to show how hydrogen diffuses towards the point of maximum hydrostatic stress.

6.2. Macroscopic Variables Governing the Microscopic Phenomenon of HAMD in Pearlitic Steel

Among the macroscopic variables governing the microscopic phenomenon of HAMD in pearlitic steel, the hydrostatic stress plays a relevant role in hydrogen transport by diffusion [64], cf. Equations (1)–(3) and thus the hydrostatic stress distributions in the samples were obtained by a numerical procedure. The finite element method (FEM) with an elastic-plastic code was applied using a Von Mises yield surface with an incompressible constitutive equation.

The FEM analysis showed that the hydrostatic stress distributions in the specimens evolved during the experiments (HE tests), reaching rising values as the loading level increases: however, in spite of such an evolution during the loading process, the point of maximum hydrostatic stress in the specimens always remains at depth x_S (characteristic of the geometry) from the notch tip, and such a point is the location towards which hydrogen is driven by stress-assisted diffusion.

In the case of the shallowly-notched geometries A (sharp notch) and C (blunt notch), the aforementioned characteristic depth x_S is relatively small, it being x_S (A) < x_S (C), i.e., hydrogen is driven to a location close to the notch tip. This suggests that a small penetration distance for the chemical species (hydrogen) is required in this case to produce the damaging embrittlement effect, so that in these shallowly-notched geometries hydrogen's deleterious effects on the pearlitic steel (HE or HD at the macro-scale, HAMD at the micro-scale) is localized in the vicinity close to the notch tip.

In the case of the deeply-notched geometries B (sharp notch) and D (blunt notch), the location of the point of maximum hydrostatic stress is located just at the specimen axis, and thus hydrogen is "pumped" towards this point by long-term stress-assisted diffusion. This suggests that a relatively large penetration distance for the chemical species (hydrogen) is required in this case to produce the damaging embrittlement effect, so that in these deeply notched geometries hydrogen's deleterious effects on the pearlitic steel (HE or HD at the macro-scale, HAMD at the micro-scale) are extended in volume.

The MFMs for different applied displacement rates (distinct HE test durations) shows that there are limit (*asymptotic*) size values of the HAMD region (consisting of different sub-modes such as oriented TTS, non-oriented TTS, quasi-MVC and cleavage, some of them disappearing in certain specific cases). To this end, it is useful to define the depth of the HAMD region as x_{HAMD} (measured from the notch tip in a radial direction of the sample, i.e., in the main direction of hydrogen transport by diffusion).

In the case of very short tests with very low embrittlement time, the asymptotic value of x_{HAMD} for such *quasi-instantaneous tests* is not negligible. This fact demonstrates that the embrittlement effect of hydrogen is detectable even for very short durations of the HE test. It is possible to write:

$$\lim_{t\to 0} x_{\mathrm{HAMD}} = \lim_{\dot{\varepsilon}\to\infty} x_{\mathrm{HAMD}} = x_0;\ x_0 = x_0(\text{geometry}) \tag{4}$$

where t is the test duration and $\dot{\varepsilon}$ represents the strain rate in the test (measured as global strain rate, applied displacement rate or extension rate). In this case, the boundary condition for hydrogen transport by diffusion (partial differential equation) is reached almost instantaneously, i.e., both hydrogen adsorption (at the outer boundary Γ^{+}) and hydrogen absorption (at the inner boundary Γ^{-}) are also quasi-instantaneous.

On the other hand, in the case of very long tests with very high embrittlement time, the asymptotic value of x_{HAMD} for such *quasi-static (steady-state) tests* reaches the depth of the maximum hydrostatic stress point x_{S}. This situation corresponds to the steady-state solution of the hydrogen diffusion problem, and it is associated with a situation of equilibrium of the metal-hydrogen system when the former is free of stress and strain. Thus:

$$\lim_{t\to\infty} x_{\mathrm{HAMD}} = \lim_{\dot{\varepsilon}\to 0} x_{\mathrm{HAMD}} = x_{\mathrm{S}};\ x_{\mathrm{S}} = x_{\mathrm{S}}(\text{geometry}) \tag{5}$$

with the same meanings as above.

The hydrogen concentration in these tests is a direct function of the hydrostatic stress at each point, since the stationary solution of the diffusion differential equation is an adequate approach in this case and the equilibrium concentration of hydrogen for the stressed metal is achieved in this case at each material point.

Table 5 summarizes the depth x_{S} of the point of maximum hydrostatic stress for each geometry, i.e., the penetration distance for hydrogen diffusion assisted by stress and strain fields.

Table 5. Depth x_{S} of the point of maximum hydrostatic stress for each geometry.

Geometry	x_{S} (mm)
A	0.30
B	1.20
C	0.80
D	1.20

Table 6 includes, together with the information of the HE experiments, the values of the maximum hydrostatic stress (σ_{max}) at the critical (fracture) instant in the tests. The information contained in it is fully consistent with the triaxiality levels appearing in the Table 2: the higher the specimen triaxiality, the more elevated the maximum hydrostatic stress levels in the specific geometry, in such a manner that the notched geometries analyzed

in the present paper can be ranked according to their triaxiality levels (and related values of maximum hydrostatic stress at the critical fracture instant) in the following order: B, A, C, D.

Table 6. Maximum hydrostatic stress (σ_{max}) levels at the fracture instant of the HE tests, together with other relevant variables (of mechanical and fractographic nature) associated with the experiments.

Sample	u_R	t_C	F_H/F_0	x_{HAMD}	σ_{max}
	(m/s)	**(s)**		**(mm)**	**(MPa)**
A10	$4.79 \times 10-7$	555	0.79	0.10	917
A3	4.81×10^{-7}	570	0.80	0.10	922
A9	1.82×10^{-7}	1365	0.77	0.15	894
A4	3.68×10^{-8}	5370	0.70	0.30	817
A7	3.96×10^{-9}	39,960	0.63	0.34	735
A1	3.26×10^{-9}	48,600	0.63	0.34	735
B6	1.00×10^{-7}	720	0.86	0.20	1147
B10	1.03×10^{-7}	780	0.90	0.20	1228
B1	1.02×10^{-8}	5760	0.79	0.25	1004
B9	8.70×10^{-9}	7380	0.82	0.21	1067
B7	6.90×10^{-9}	8520	0.79	0.27	1004
B3	6.23×10^{-9}	11,160	0.85	0.30	1118
B23	6.02×10^{-10}	75,600	0.69	0.60	835
B22	1.87×10^{-10}	143,040	0.48	0.93	559
B21	1.12×10^{-10}	262,800	0.52	1.00	603
C6	1.83×10^{-6}	516	0.91	0.40	625
C8	9.71×10^{-7}	972	0.91	0.45	625
C12	3.45×10^{-7}	2295	0.87	0.40	596
C2	1.54×10^{-7}	4500	0.84	0.55	574
C11	6.67×10^{-8}	7560	0.77	0.55	528
C4	5.47×10^{-8}	8340	0.75	0.50	512
C1	5.85×10^{-9}	68,400	0.72	0.85	497
C7	5.33×10^{-9}	75,000	0.72	0.75	497
D10	2.13×10^{-7}	660	0.91	0.10	589
D3	2.06×10^{-7}	780	0.95	0.21	611
D7	4.55×10^{-8}	3240	0.92	0.33	596
D11	2.45×10^{-8}	6300	0.93	0.41	603
D5	1.49×10^{-8}	9000	0.90	0.60	581
D2	1.35×10^{-8}	9420	0.88	0.50	574
D21	6.98×10^{-10}	182,400	0.88	1.15	574
D24	3.93×10^{-10}	324,000	0.88	1.20	574

u_R: remote displacement rate. t_C: time to failure or critical time. F_H/F_0: failure load in hydrogen/failure load in air. x_{HAMD}: depth of the hydrogen-assisted micro-damage zone. $\sigma_{max:}$ maximum hydrostatic stress at the notch tip (failure instant).

7. Micromechanical Modeling of HAMD in Pearlitic Steel

7.1. HAMD by TTS in Pearlitic Steel

In order to formulate a plausible micromechanical model of HAMD by TTS in pearlitic steel, it is worth to mention the classical scientific references comprising the main micromechanical models of HE, HD, HAF (in general) or HAC (when a crack is present in the material). Beachem [65] formulated a classical model for HAC/HE in 1972 and coined the term *quasi-cleavage* to describe a kind of fractographic mode, with more or less ductile appearance, linked to hydrogen effects in material. Such a name has so frequently been used for a wide variety of damage situations that Thompson and Bernstein [66] stated that the term *quasi-cleavage* is on the verge of becoming meaningless.

More recently, two complementary terms arose in the scientific literature related to HE, HD, HAF or HAC, namely (i) *hydrogen-enhanced localized plasticity* (HELP) and (ii) *hydrogen-enhanced decohesion* (HEDE). The term HELP was firstly coined by Birnbaum

and Sofronis [67], and this idea of hydrogen-plasticity interaction has been developed by Sofronis et al. [68] and by Gerberich [69]. The idea of decohesion (with loss of fracture toughness) promoted in the material (associated with the term HEDE) appears in the classical paper by Hirth [70] and has been used by Novak et al. [71].

In recent years, Toribio [72] formulated the two possibilities of HELP and HEDE as the dual micromechanisms of HAMD in fully-pearlitic steels (in the presence of cracks) depending on their degree of cold drawing, in such a manner that in hot-rolled pearlitic steels (before cold drawing) the HAMD develops by pure TTS resembling, in a certain sense, the *Michelangelo stone sculpture texture* (MSST) whereas, on the other hand, heavily cold-drawn pearlitic steel wires with cracks exhibit anisotropic HE behavior with crack deflection, and a micromechanism of HAMD developing by enlarged and oriented TTS (EOTTS) and resembling the *Donatello wooden sculpture texture* (DWST). While the first case (hot rolled pearlite) that fractures in hydrogen by TTS may be classified as HELP, the second one (cold drawn pearlite) that fractures in hydrogen by EOTTS could be denoted, more properly, as HEDE.

In ferritic-pearlitic steels used in pipelines, the dual roles of pearlite microstructure to interfere/facilitate gaseous hydrogen-assisted fatigue crack growth has been studied [73] and two micromechanisms of damage as *pearlite tearing* (PT) and *pearlite delamination* (PD) are proposed in the pearlite phase under the combined action of cyclic loading (fatigue) and hydrogen atmosphere. PT could be similar to TTS (a sort of HELP) analyzed in this paper whereas PD could be similar to EOTTS (a kind of HEDE) using the terminology of the present paper.

Since the present paper is focused on hot rolled pearlitic steel (isotropic) in the absence of any cold drawing, the *macro*-, *micro*- and *nano*-mechanical features observed in the HAMD allow an analysis of the *macro*-, *micro*- and *nano*-mechanism of fracture, but *without* considering any anisotropic effects on HE behavior caused by an oriented microstructural arrangement promoted by cold drawing.

In this framework, it can be assured that the TTS topography, associated with HE/HD in pearlite, exhibits certain evidence of hydrogen-plasticity interactions in the form of a sort of *micro*-tearing or *nano*-tearing at a scale below the pearlite interlamellar spacing of the material, and this TTS (a type of HAMD) may be classified as a HELP due to local ductile feature and hydrogen-plasticity interactions at the *micro*- and *nano*-scale.

With regard to the *macro*-scale, the TTS fractographic mode represents a subcritical hydrogen-assisted fracture mode associated with the stage II or plateau in the CGK curve da/dt-K in which the CGR is independent of the SIF K. The CGR during TTS crack propagation was measured in constant strain tests (CSTs) by standard optical methods using pre-cracked prismatic three-point bend specimens, cf. [74], obtaining a value of CGR v = 10^{-7} m/s (Figure 11). In notched specimens, the TTS mode represents a sub-critical post-crack prolonging the original notch and growing at the CGR of 10^{-7} m/s.

Again, in the matter of the *macro*-scale, the depth of the TTS region allows a kinematic formulation of a fracture criterion on the basis of the *local strain rate at the notch tip* or *notch tip strain rate* (NTSR), as explained in [75]. The NTSR is the representative *local kinematic variable* governing the HE process in the vicinity of the notch tip, in contrast with the *global kinematic variable* of the specimen, the global displacement rate or crosshead speed, cf. Table 3. There are two asymptotic situations: the *ultra-fast tests* (very high local strain rate) and the *quasi-static tests* (extremely low local strain rate). The first is fast enough to avoid hydrogen diffusion towards the inner points of the sample, whereas the second is slow enough to allow the stationary condition for the hydrogen diffusion problem to be reached (where $x_{TTS} = x_S$).

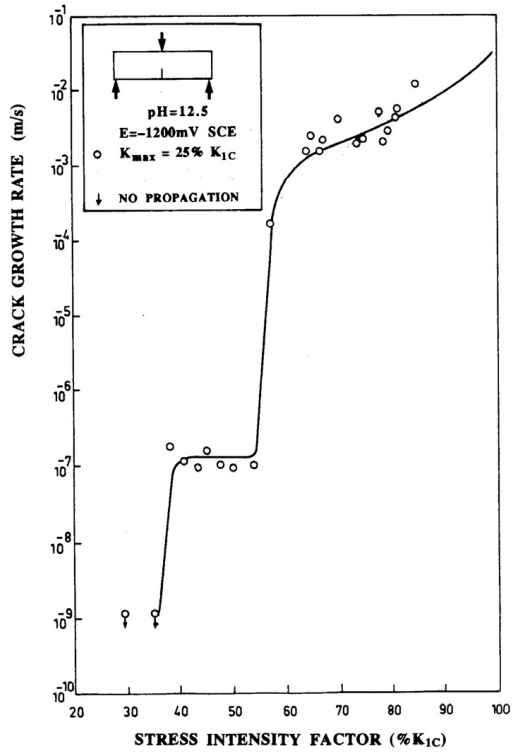


Figure 11. Crack growth kinetics curve (da/dt-K) for a high-strength eutectoid pearlitic steel. The stage II (*plateau*) is associated with a crack growth rate (CGR) of 10^{-7} m/s and TTS fracture mode.

In the *quasi-static tests* (horizontal dashed lines in Figure 12) the critical equivalent stress in hydrogen environment (defined in [75]) reaches an asymptotic value different for each geometry, and dependent on the triaxiality level shown in Table 2: the higher the triaxiality level, the lower the dimensionless fracture stress in the tests.

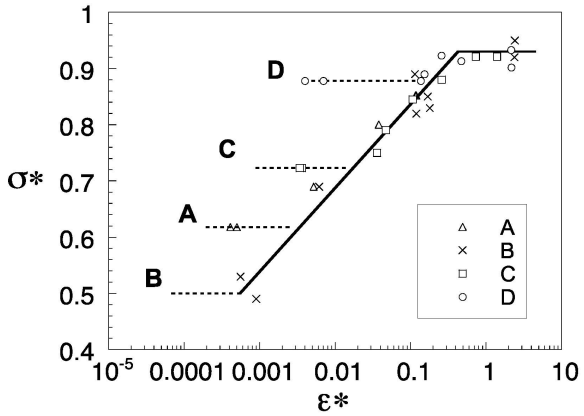


Figure 12. Results of the SSRT on notched samples under HE environmental conditions, plotted in kinematic terms: *dimensionless fracture stress* as a function of the *notch tip strain rate* (NTSR), data from [75]. The asterisk is used to indicate a dimensionless variable.

7.2. Evolution (Sub-Modes) of HAMD in Pearlitic Steel

In order to formulate a plausible micromechanical model of evolution of HAMD in pearlitic steel, Tables 4 and 5 are the keystones. On one hand, Table 4 contains the different sub-modes of HAMD and, on the other hand, Table 5 contains mechanical characteristics of each specific sample geometry: the depth of the maximum hydrostatic stress point towards

which hydrogen diffuses, i.e., the *hydrogen penetration path* (HPP), a sort of *chemical path* that later produces a *mechanical path*, the *crack path* (CP) itself.

With regard to the *micro*-mechanism of formation of HAMD, the pearlitic lamellar microstructure could fail at the *micro*-scale either by *trans-lamellar cracking path* (TLCP) or by *inter-lamellar cracking path* (ILCP). The first one requires the fracture of cementite lamellae, that could happen according to the Miller-Smith micro-mechanism [76] of *shear cracking of pearlite* (SCP), represented in Figure 13.

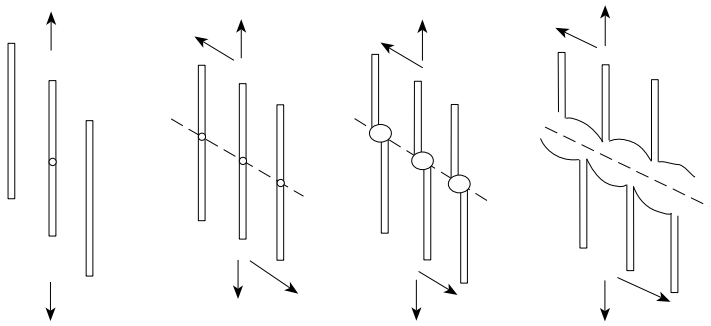


Figure 13. Miller-Smith mechanism of shear cracking in pearlite (SCP).

Figure 14 shows a micromechanical model of HAMD (mainly TTS) in pearlitic steels with a lamellar microstructure: (a) *trans-lamellar cracking path* (TLCP) consisting of either *pearlite tearing* (PT) [73] or *shear cracking of pearlite* (SCP) [76], i.e., a sort of HELP; (b) *inter-lamellar cracking path* (ILCP) consisting of pearlite delamination (PD) [73], i.e., a sort of HEDE. Probably both are operative at the *micro*- and *nano*-scale and a combination of them could take place. In addition, in these *micro*- and *nano*-levels, hydrogen transport by dislocations [77–81] would be operative over distances below the pearlite interlamellar spacing (*nano*-scale). At the *macro*-scale, stress-and-strain-assisted diffusion of hydrogen predominates in pearlite over the hydrogen transport by dislocations [82].

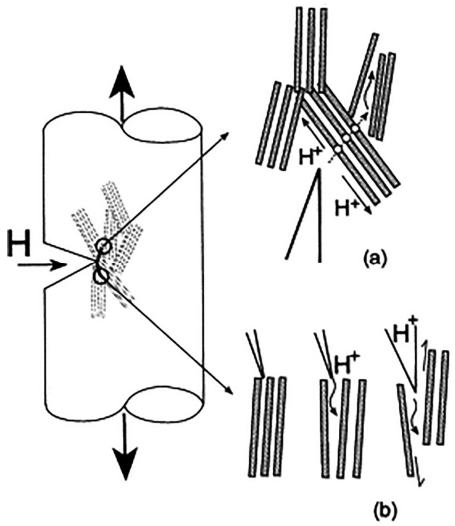


Figure 14. Micromechanical model of HAMD (TTS) in pearlitic steels with lamellar microstructure: (**a**) *trans-lamellar cracking path* (TLCP) consisting of either PT or SCP, data from [73,76], i.e., a sort of HELP; (**b**) *inter-lamellar cracking path* (ILCP) consisting of PD, data from [73], i.e., a sort of HEDE.

Figure 15 plots the HAMD depth (x_{HAMD}) as a function of the time to failure (tc) (*embrittlement time*) in the HE tests with notched samples A, B, C and D; variables are

expressed in dimensionless terms, i.e., divided by their respective values in the very slow quasi-static test of each geometry ($x_{HAMD,\infty}$ and $t_{c,\infty}$).

An increasing trend of the HAMD depth with the embrittlement time is observed, i.e., the longer the HE, the deeper the area damaged by hydrogen at the micro- and nano-levels as a consequence of hydrogen transport over macroscopic distances by a mechanism of diffusion assisted by stress and strain fields.

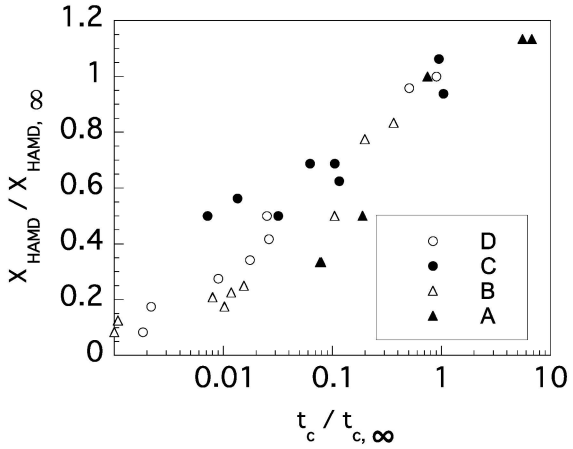


Figure 15. Relationship between the HAMD depth (x_{HAMD}) and the time to failure (tc) or *embrittlement time* in HE tests with notched samples A, B, C and D. Variables are divided by their respective values in the quasi-static test of each geometry ($x_{HAMD,\infty}$ & $t_{c,\infty}$).

In the matter of the quasi-MVC micro-fracture mode, it appears *only* in those notched geometries in which the HPP is long if compared with the HE test duration, i.e., when the hydrogen does not have enough time to reach the prospective fracture location (maximum hydrostatic stress point). This happens in deeply-notched geometries B (sharp) and D (blunt), since in these two the maximum hydrostatic stress appears at the geometry center or sample axis. The quasi-MVC topography also appears in short HE tests using shallowly-notched blunt geometry C in which the maximum hydrostatic stress is at a certain distance from the notch tip.

Then, the quasi-MVC area could be a candidate to the TTS zone that does not reach such a condition because of an insufficient level of hydrogenation. On the other hand, in HE tests using the shallowly notched sharp geometry A (either slow or quick), the HPP is very small, so that hydrogen has enough time to reach the near-tip location of the maximum hydrostatic stress point. The same happens in the slow HE tests with the shallowly-notched blunt geometry C (in this case the HPP is a little bit longer but the test is slow enough to allow the hydrogen to reach the critical location).

With regard to the pure MVC geometry, it takes place in regions of low triaxiality level that fail in ductile manner. When HAMD progresses in the form of a TTS crack extending the original notch, the local increase in triaxiality could produce the quasi-MVC topography after the TTS and before the MVC, the quasi-MVC being a consequence of a higher triaxiality level (near the TTS crack tip) when compared with the lower triaxiality level in the MVC region. Finally, when the macro-crack (TTS plus quasi-MVC in some cases plus MVC) reaches a critical size, final catastrophic failure takes place by cleavage.

8. Conclusions

The evolution of HAMD was analyzed, firstly showing an oriented TTS mode that turns to non-oriented (or randomly-oriented) TTS and finally to a quasi-MVC topography before final fracture by cleavage (purely mechanical) takes place.

The TTS represents a sort of HELP mode in which *local micro*- and *nano*-damage takes place in the form of hydrogen-plasticity interactions and dislocation transport of hydrogen developing at a very fine scale of analysis.

Although the main mechanism of hydrogen transport in pearlite is diffusion assisted by stress and strain fields at the *macro*-scale, hydrogen transport by dislocational movement (dragging) could be operative at the *micro*- and *nano*-scale.

At the *micro*-level, the formation of TTS could involve an interplay also between HELP and HEDE in the form of *pearlite tearing* (PT) as a mode of HELP or, on the other hand, in the form of *pearlite delamination* (PD) as a mode of HEDE.

In the case of a local phenomenon of HELP by PT to create TTS, the Miller-Smith mechanism of *shear cracking of pearlite* (SCP) could be operative in this case, with breaking of brittle cementite lamellae by local shear of ductile ferrite bands.

The locally-ductile micro-mechanism of PT or SCP (a mode of HELP) produces a *trans-lamellar cracking path* (TLCP), whereas the locally-brittle micro-mechanism of PD (a mode of HEDE) produces an *inter-lamellar cracking path* (ILCP).

The TTS fractographic mode represents a subcritical hydrogen-assisted fracture mode associated with the stage II or plateau in the CGK curve da/dt-K in which the CGR is independent of the SIF K.

The CGR during TTS crack propagation was measured in pre-cracked samples of pearlitic steel under constant strain tests (CSTs), with a value of CGR v = 10^{-7} m/s for hydrogen-assisted sub-critical cracking by TTS.

The TTS appears in strongly-hydrogenated areas, whereas the pseudo-MVC areas (transition regions) correspond to weakly-hydrogenated zones, as demonstrated by comparing the HPP to the maximum hydrostatic stress point and the HE test duration.

The quasi-MVC topography could be considered as a candidate to TTS that becomes TTS itself when a sufficient amount of hydrogen penetrates this zone of sub-critical hydrogen-assisted cracking/fracture.

Funding: This research was funded by the following Spanish Institutions: Ministry for Science and Technology (MICYT; Grant MAT2002-01831), Ministry for Education and Science (MEC; Grant BIA2005-08965), Ministry for Science and Innovation (MICINN; Grant BIA2008-06810) and finally Ministry for Economy and Competitiveness (MINECO; Grant BIA2011-27870). In addition, complementary funds were provided by the Regional Government *Junta de Castilla y León* (JCyL; Grants SA067A05, SA111A07 and SA039A08).

Institutional Review Board Statement: Not applicable.

Informed Consent Statement: Not applicable.

Data Availability Statement: Data is contained within the article.

Acknowledgments: The article was written during a very busy year of 2023. The author wishes to warmly dedicate it to his wife Lourdes Menárguez, his daughter Ana Lym Toribio and his son Juan Sun Toribio for the love, patience and support they have always provided and for very joyful moments between the rigorous and exhausting scientific work.

Conflicts of Interest: The author declares no conflict of interest. With regard to the research funds, the different institutions providing financial support for the scientific research had no role in the design of the study; in the collection, analyses, or interpretation of data; in the writing of the present manuscript; and in the decision to publish the results.

References

1. Masoumi, M.; Echeverri, E.A.A.; Tschiptschin, A.P.; Goldenstein, H. Improvement of wear resistance in a pearlitic rail steel via quenching and partitioning processing. *Sci. Rep.* **2019**, *9*, 7454. [CrossRef] [PubMed]
2. Ferreira, V.M.; Mecozzi, M.G.; Petrov, R.H.; Sietsma, J. Microstructure development of pearlitic railway steels subjected to fast heating. *Mater. Des.* **2022**, *221*, 110989. [CrossRef]
3. Toribio, J. On the intrinsic character of the stress-strain curve of a prestressing steel. *J. Testing Eval.* **1992**, *20*, 357–362.
4. Toribio, J. Cold drawn eutectoid pearlitic steel wires as high performance materials in structural engineering. *Struct. Integr. Health Monit.* **2006**, *2*, 239–247.

5. Borchers, C.; Kirchheim, R. Cold-drawn pearlitic steel wires. *Prog. Mater. Sci.* **2016**, *82*, 405–444. [CrossRef]
6. Yan, W.; Chen, W.; Li, J. Quality control of high carbon steel for steel wires. *Materials* **2019**, *12*, 846. [CrossRef]
7. Mihaliková, M.; Lišková, A.; Hagarová, M.; Cervová, J. Damage pearlitic steel in operation. *Procedia Eng.* **2017**, *190*, 352–356. [CrossRef]
8. Embury, J.D.; Fisher, R.M. The structure and properties of drawn pearlite. *Acta Metall.* **1966**, *14*, 147–159. [CrossRef]
9. Langford, G. Deformation of Pearlite. *Metall. Trans. A* **1977**, *8*, 861–875. [CrossRef]
10. Ridley, N. A review of the data on the interlamellar spacing of pearlite. *Metall. Trans. A* **1984**, *15*, 1019–1036. [CrossRef]
11. Lewandowski, J.J.; Thompson, A.W. Effects of the prior austenite grain size on the ductility of fully pearlitic eutectoid steel. *Metall. Trans. A* **1986**, *17*, 461–472. [CrossRef]
12. Nam, W.J.; Bae, C.M. Void initiation and microstructural changes during wire drawing of pearlitic steels. *Mater. Sci. Eng. A* **1995**, *203*, 278–285. [CrossRef]
13. Read, H.G.; Reynolds, W.T., Jr.; Hono, K.; Tarui, T. AFPIM and TEM studies of drawn pearlitic wire. *Scr. Mater.* **1997**, *37*, 1221–1230. [CrossRef]
14. Toribio, J.; Ovejero, E. Microstructure evolution in a pearlitic steel subjected to progressive plastic deformation. *Mater. Sci. Eng. A* **1997**, *234–236*, 579–582. [CrossRef]
15. Toribio, J.; Ovejero, E. Effect of cumulative cold drawing on the pearlite interlamellar spacing in eutectoid steel. *Scr. Mater.* **1998**, *39*, 323–328. [CrossRef]
16. Toribio, J.; Ovejero, E. Microstructure orientation in a pearlitic steel subjected to progressive plastic deformation. *J. Mater. Sci. Lett.* **1998**, *17*, 1037–1040. [CrossRef]
17. Toribio, J.; Ovejero, E. Effect of cold drawing on microstructure and corrosion performance of high-strength steel. *Mech. Time-Depend. Mater.* **1998**, *1*, 307–319. [CrossRef]
18. Languillaume, J.; Kapelski, G.; Baudelet, B. Cementite dissolution in heavily cold drawn pearlitic steel wires. *Acta Mater.* **1997**, *45*, 1201–1212. [CrossRef]
19. Nam, W.J.; Bae, C.M.; Oh, S.J.; Kwon, S.J. Effect of interlamellar spacing on cementite dissolution during wire drawing of pearlitic steel wires. *Scr. Mater.* **2000**, *42*, 457–463. [CrossRef]
20. Choi, H.C.; Park, K.T. The effect of carbon content on the Hall-Petch parameter in the cold drawn hypereutectoid steels. *Scr. Mater.* **1996**, *34*, 857–862. [CrossRef]
21. Nam, W.J.; Bae, C.M.; Lee, C.S. Effect of carbon content on the Hall-Petch parameter in cold drawn pearlitic steel wires. *J. Mater. Sci.* **2002**, *37*, 2243–2249. [CrossRef]
22. Toribio, J. Relationship between microstructure and strength in eutectoid steels. *Mater. Sci. Eng. A* **2004**, *387–389*, 227–230. [CrossRef]
23. Toribio, J.; González, B.; Matos, J.C. Microstructure and mechanical properties in progressively drawn pearlitic steel. *Mater. Trans.* **2014**, *55*, 93–98. [CrossRef]
24. Tarui, T.; Maruyama, N.; Takahashi, J.; Nishida, S.; Tashiro, H. Microstructure control and strengthening of high-carbon steel wires. *Nippon Steel Tech. Rep.* **2005**, *91*, 56–61.
25. Shiota, Y.; Tomota, Y.; Moriai, A.; Kamiyama, T. Structure and mechanical behavior of heavily drawn pearlite and martensite in a high carbon steel. *Met. Mater. Int.* **2005**, *11*, 371–376. [CrossRef]
26. Zhang, X.; Godfrey, A.; Huang, X.; Hansen, N.; Liu, Q. Microstructure and strengthening mechanisms in cold-drawn pearlitic steel wire. *Acta Mater.* **2011**, *59*, 3422–3430. [CrossRef]
27. Zhang, X.; Godfrey, A.; Hansen, N.; Huang, X. Hierarchical structures in cold-drawn pearlitic steel wire. *Acta Mater.* **2013**, *61*, 4898–4909. [CrossRef]
28. Li, Y.J.; Choi, P.; Goto, S.; Borchers, C.; Raabe, D.; Kirchheim, R. Evolution of strength and microstructure during annealing of heavily cold-drawn 6.3 GPa hypereutectoid pearlitic steel wire. *Acta Mater.* **2012**, *60*, 4005–4016. [CrossRef]
29. Takahashi, J.; Kosaka, M.; Kawakami, K.; Tarui, T. Change in carbon state by low-temperature aging in heavily drawn pearlitic steel wires. *Acta Mater.* **2012**, *60*, 387–395. [CrossRef]
30. Zhao, T.Z.; Zhang, S.H.; Zhang, G.L.; Song, H.W.; Cheng, M. Hardening and softening mechanisms of pearlitic steel wire under torsion. *Mater. Des.* **2014**, *59*, 397–405. [CrossRef]
31. Rastegari, H.; Kermanpur, A.; Najafizadeh, A. Effect of initial microstructure on the work hardening behavior of plain eutectoid steel. *Mater. Sci. Eng. A* **2015**, *632*, 103–109. [CrossRef]
32. Porter, D.A.; Easterling, K.E.; Smith, G.D.W. Dynamic studies of the tensile deformation and fracture of pearlite. *Acta Metall.* **1978**, *26*, 1405–1422. [CrossRef]
33. Hyzak, J.M.; Bernstein, I.M. The role of microstructure on the strength and toughness of fully pearlitic steels. *Metall. Trans. A* **1976**, *7*, 1217–1224. [CrossRef]
34. Park, Y.J.; Bernstein, I.M. The process of crack initiation and effective grain size for cleavage fracture in pearlitic eutectoid steel. *Metall. Trans. A* **1979**, *10*, 1653–1664. [CrossRef]
35. Alexander, D.J.; Bernstein, I.M. The cleavage plane of pearlite. *Metall. Trans. A* **1982**, *13*, 1865–1868. [CrossRef]
36. Dollar, M.; Bernstein, I.M.; Thompson, A.W. Influence of deformation substructure on flow and fracture of fully pearlitic steel. *Acta Metall.* **1988**, *36*, 311–320. [CrossRef]

37. Toribio, J.; Ayaso, F.J.; González, B.; Matos, J.C.; Vergara, D.; Lorenzo, M. Tensile fracture behavior of progressively-drawn pearlitic steels. *Metals* **2016**, *6*, 114. [CrossRef]
38. Zhao, T.Z.; Zhang, G.L.; Zhang, S.H.; Zhang, L.Y. Fracture characteristics of fully pearlitic steel wire in tension and torsion. *J. Iron Steel Res. Int.* **2016**, *23*, 1206–1212. [CrossRef]
39. Zhao, T.Z.; Zhang, G.L.; Zhang, S.H.; Zhang, L.Y. Influence of lamellar direction in pearlitic steel wire on mechanical properties and microstructure evolution. *J. Iron Steel Res. Int.* **2016**, *23*, 1290–1296. [CrossRef]
40. Khiratkar, V.N.; Mishra, K.; Srinivasulu, P.; Singh, A. Effect of inter-lamellar spacing and test temperature on the Charpy impact energy of extremely fine pearlite. *Mater. Sci. Eng. A* **2019**, *754*, 622–627. [CrossRef]
41. Lu, X. Correlation between microstructural evolution and mechanical properties of 2000 MPa cold-drawn pearlitic steel wires during galvanizing simulated annealing. *Metals* **2019**, *9*, 326. [CrossRef]
42. Jung, J.Y.; An, K.S.; Park, P.Y.; Nam, W.J. Correlation between microstructures and ductility parameters of cold drawn hyper-eutectoid steel wires with different drawing strains and post-deformation annealing conditions. *Metals* **2021**, *11*, 178. [CrossRef]
43. Lynch, S.P. Failures of structures and components by environmentally assisted cracking. *Eng. Fail. Anal.* **1994**, *1*, 77–90. [CrossRef]
44. Toribio, J.; Elices, M. Influence of residual stresses on hydrogen embrittlement susceptibility of prestressing steels. *Int. J. Solids Struct.* **1991**, *28*, 791–803. [CrossRef]
45. Lillard, R.S.; Enos, D.G.; Scully, J.R. Calcium hydroxide as a promoter of hydrogen absorption in 99.5% Fe and a fully pearlitic 0.8% C steel during electrochemical reduction of water. *Corrosion* **2000**, *56*, 1119–1132. [CrossRef]
46. Enos, D.G.; Scully, J.R. A critical-strain criterion for hydrogen embrittlement of cold-drawn, ultrafine pearlitic steel. *Metall. Mater. Trans. A* **2002**, *33*, 1151–1166. [CrossRef]
47. Proverbio, E.; Longo, P. Sub critical crack growth in hydrogen assisted cracking of cold drawn eutectoid steel. *Corros. Sci.* **2007**, *49*, 2421–2435. [CrossRef]
48. Toribio, J.; Ovejero, E. Hydrogen assisted cracking in progressively drawn pearlitic steel. *Corros. Sci.* **2007**, *49*, 3539–3556. [CrossRef]
49. Mallick, A.; Das, S.; Mathur, J.; Bhattacharyya, T.; Dey, A. Internal reversible hydrogen embrittlement leads to engineering failure of cold drawn wire. *Case Stud. Eng. Fail. Anal.* **2013**, *1*, 139–143. [CrossRef]
50. Nakamura, S.-I.; Suzumura, K. Hydrogen embrittlement and corrosion fatigue of corroded bridge wires. *J. Constr. Steel Res.* **2009**, *65*, 269–277. [CrossRef]
51. Vehovar, L.; Kuhar, V.; Vehovar, A. Hydrogen-assisted stress-corrosion of prestressing wires in a motorway viaduct. *Eng. Fail. Anal.* **1998**, *5*, 21–27. [CrossRef]
52. Perrin, M.; Gaillet, L.; Tessier, C.; Idrissi, H. Hydrogen embrittlement of prestressing cables. *Corros. Sci.* **2010**, *52*, 1915–1926. [CrossRef]
53. Thompson, A.W.; Chesnutt, J.C. Identification of a fracture mode: The tearing topography surface. *Metall. Trans. A* **1982**, *10*, 379–405. [CrossRef]
54. Costa, J.E.; Thompson, A.W. Hydrogen cracking in nominally pearlitic 1045 steel. *Metall. Trans. A* **1982**, *13*, 1315–1318. [CrossRef]
55. Toribio, J.; Lancha, A.M.; Elices, M. Characteristics of the new tearing topography surface. *Scr. Metall. Mater.* **1991**, *25*, 2239–2244. [CrossRef]
56. Toribio, J.; Lancha, A.M.; Elices, M. The tearing topography surface as the zone associated with hydrogen embrittlement processes in pearlitic steel. *Metall. Trans. A* **1992**, *23*, 1573–1584. [CrossRef]
57. Toribio, J.; Vasseur, E. Hydrogen-assisted micro-damage evolution in pearlitic steel. *J. Mater. Sci. Lett.* **1997**, *16*, 1345–1348. [CrossRef]
58. Toribio, J. Fracture mechanics approach to hydrogen-assisted microdamage in eutectoid steel. *Metall. Mater. Trans. A* **1997**, *28*, 191–197. [CrossRef]
59. Toribio, J. Time-dependent triaxiality effects on hydrogen-assisted microdamage evolution in pearlitic steel. *ISIJ Int.* **2012**, *52*, 228–233. [CrossRef]
60. Toribio, J. Triaxiality effects on hydrogen-assisted micro-damage (HAMD), notch tensile strength and hydrogen embrittlement of pearlitic steel. *Procedia Struct. Integr.* **2021**, *33*, 1139–1145. [CrossRef]
61. Wang, M.; Akiyama, E.; Tsuzaki, K. Crosshead speed dependence of the notch tensile strength of a high strength steel in the presence of hydrogen. *Scr. Mater.* **2005**, *53*, 713–718. [CrossRef]
62. Wang, M.; Akiyama, E.; Tsuzaki, K. Effect of hydrogen on the fracture behavior of high strength steel during slow strain rate test. *Corros. Sci.* **2007**, *49*, 4081–4097. [CrossRef]
63. Toribio, J. Macro-and micro-approach to the notch-induced fracture process and notch tensile strength in eutectoid hot-rolled pearlitic steel: *Weakest link versus process zone fracture criterion*. *Procedia Struct. Integr.* **2021**, *33*, 1131–1138. [CrossRef]
64. Toribio, J.; Kharin, V. A generalised model of hydrogen diffusion in metals with multiple trap types. *Phil. Mag.* **2015**, *95*, 3429–3451. [CrossRef]
65. Beachem, C.D. A new model for hydrogen-assisted cracking (hydrogen "embrittlement"). *Metall. Trans B* **1972**, *3*, 441–455. [CrossRef]

66. Thompson, A.W.; Bernstein, I.M. The role of plastic fracture processes in hydrogen embrittlement. In *Fracture 1977: Advances in Resesearch on the Strength and Fracture of Materials*; Taplin, D.M.R., Ed.; Pergamon Press: New York, NY, USA, 1977; pp. 249–254.
67. Birnbaum, H.K.; Sofronis, P. Hydrogen-enhanced localized plasticity—A mechanism for hydrogen-related fracture. *Mater. Sci. Eng. A* **1994**, *176*, 191–202. [CrossRef]
68. Sofronis, P.; Liang, Y.; Aravas, N. Hydrogen induced shear localization of the plastic flow in metals and alloys. *Eur. J. Mech.-A/Solids* **2001**, *20*, 857–872. [CrossRef]
69. Gerberich, W. Modeling hydrogen induced damage mechanisms in metals. In *Gaseous Hydrogen Embrittlement of Materials in Energy Technologies*; Woodhead Publishing: Sawston, UK, 2012; pp. 209–246.
70. Hirth, J.P. Effects of hydrogen on the properties of iron and steel. *Metall. Trans. A* **1980**, *11*, 861–890. [CrossRef]
71. Novak, P.; Yuan, R.; Somerday, B.P.; Sofronis, P.; Ritchie, R.O. A statistical, physical-based, micro-mechanical model of hydrogen-induced intergranular fracture in steel. *J. Mech. Phys. Solids* **2010**, *58*, 206–226. [CrossRef]
72. Toribio, J. HELP *versus* HEDE in progressively cold-drawn pearlitic steels: *Between Donatello and Michelangelo*. *Eng. Fail. Anal.* **2018**, *94*, 157–164. [CrossRef]
73. Ogawa, Y.; Nishida, H.; Nakamura, M.; Olden, V.; Vinogradov, A.; Matsunaga, H. Dual roles of pearlite microstructure to interfere/facilitate gaseous hydrogen-assisted fatigue crack growth in plain carbon steels. *Int. J. Fatigue* **2022**, *154*, 106561. [CrossRef]
74. Toribio, J. A fracture mechanics approach to hydrogen assisted microdamage and failure analysis of high-strength pearlitic steel wires: *Resembling Michelangelo Stone Sculpture Texture*. *Procedia Struct. Integr.* **2022**, *41*, 724–727. [CrossRef]
75. Toribio, J. Hydrogen embrittlement of pearlitic steel in the presence of notches: A kinematic fracture criterion based on the notch tip strain rate. *Procedia Struct. Integr.* **2022**, *41*, 736–743. [CrossRef]
76. Miller, L.E.; Smith, G.C. Tensile fracture in carbon steels. *J. Iron Steel Inst.* **1970**, *208*, 998–1005.
77. Tien, J.; Thompson, A.W.; Bernstein, I.M.; Richards, R.J. Hydrogen transport by dislocations. *Metall. Trans A* **1976**, *7*, 821–829. [CrossRef]
78. Dadfarnia, M.; Martin, M.L.; Nagao, A.; Sofronis, P.; Robertson, I.M. Modeling hydrogen transport by dislocations. *J. Mech. Phys. Solids* **2015**, *78*, 511–525. [CrossRef]
79. Vermeij, T.; Hoefnagels, J.P.M. Plasticity, localization, and damage in ferritic-pearlitic steel studied by nanoscale digital image correlation. *Scr. Mater.* **2022**, *208*, 114327. [CrossRef]
80. Yang, C.D.; Liu, Y.; Zhou, G.Y.; Zou, X.L.; Lu, X.G.; Cao, G.H. Microstructural evolution of SK85 pearlitic steel deformed by heavy cold rolling. *Materials* **2022**, *15*, 8405. [CrossRef] [PubMed]
81. Bhadeshia, H.K.D.H.; Chintha, A.R. Critical assessment: The strength of undeformed pearlite. *Mater. Sci. Tech.* **2022**, *38*, 1291–1299. [CrossRef]
82. Toribio, J.; Kharin, V. Fractographic and numerical study of hydrogen–plasticity interactions near a crack tip. *J. Mater. Sci.* **2006**, *41*, 6015–6025. [CrossRef]

Disclaimer/Publisher's Note: The statements, opinions and data contained in all publications are solely those of the individual author(s) and contributor(s) and not of MDPI and/or the editor(s). MDPI and/or the editor(s) disclaim responsibility for any injury to people or property resulting from any ideas, methods, instructions or products referred to in the content.